Feng, W., Li, Z., Hoey, T., Zhang, Y., Wang, R., Samsonov, S., Li, Y., Xu, Z. (2014): Patterns and mechanisms of coseismic and postseismic slips of the 2011 MW 7.1 Van (Turkey) earthquake revealed by multi-platform synthetic aperture radar interferometry. - *Tectonophysics*, *632*, p. 188-198.

DOI: http://doi.org/10.1016/j.tecto.2014.06.011

Patterns and Mechanisms of Coseismic and Postseismic Slips of the 2011 MW 7.1 Van (Turkey) Earthquake Revealed by Multi-platform Synthetic Aperture Radar Interferometry

Wanpeng Feng (1,2), Zhenhong Li(3), Trevor Hoey(2), Yong Zhang(4,5), Rongjiang Wang(4), Sergey Samsonov(6) , Yongsheng Li(7), and Zhonghuai Xu(1)

1: Institute of Geophysics, China Earthquake Administration, Beijing, 100081, China

2: COMET, School of Geographical and Earth Sciences, University of Glasgow, Glasgow, G12 8QQ, UK.

3: COMET, School of Civil Engineering and Geosciences, Newcastle University, Newcastle upon Tyne, NE1 7RU, UK

4: GFZ German Research Centre for Geosciences, D-14473 Potsdam, Germany

5: Department of Geophysics, School of Earth and Space Sciences, Peking University, Beijing 100871, China

6: Canada Centre for Remote Sensing, Natural Resources Canada, Ottawa, ON K1A0Y7, Canada

7: Institute of Crustal Dynamics, China Earthquake Administration, Beijing, 100085, China

Abstract

On 23rd October 2011, a M_W 7.1 reverse slip earthquake occurred in the Bardakçı-Saray thrust fault zone in the Van region, Eastern Turkey. Earlier geodetic studies have found different slip distributions in terms of both magnitude and pattern. In this paper, we present several COSMO-SkyMED (CSK), Envisat ASAR and RADARSAT-2 interferograms spanning different time intervals, showing that significant postseismic signals can be observed in the first three days after the mainshock. Using observations that combine coseismic and postseismic signals is shown to significantly underestimate coseismic slip. We hence employed the CSK pair with the minimum postseismic signals to generate one conventional interferogram and one along-track interferogram for further coseismic modelling. Our best-fit coseismic slip model suggests that: (1) this event is associated with a buried NNW dipping fault with a preferable dip angle of 49º and a maximum slip of 6.5 m at a depth of 12 km; and (2) two unequal asperities can be observed, consistent with previous seismic solutions. Significant oblique aseismic slip with predominant left-lateral slip components above the coseismic rupture zone within the first 3 days after the mainshock is also revealed by a postseismic CSK interferogram, indicating that the greatest principal stress axis might have rotated due to a significant stress

drop during the coseismic rupture.

Keywords:

Van Earthquake; Coseismic Modelling; InSAR Inversion; Topographic Effects; Afterslip modelling

1. Introduction

On 23rd October 2011, a M_W 7.1 thrust fault earthquake occurred 30 km north of Van, western Turkey. This event occurred in the Bardakçı-Saray thrust fault zone (Doğan and Karakaş, 2013), north of the Bitlis-Zagors Suture belt, one of the most tectonically active areas on Earth which has undergone crustal shortening and thickening as a result of the collisions between Arabian and Eurasian plates (Figure 1(a)) (Aksoy et al., 2005; Dewey and Pindell, 1985). GPS-derived horizontal velocity fields indicate a general counterclockwise rotation in the region including the Bitlis-Zagros fold belt at the rate of ~20-30 mm/a near the epicentre (Relinger et al., 2006) (Figure 1). A series of large strike-slip historical earthquakes along the boundaries of the Anatolian plateau imply that the major strike-slip faults (both the Northern Anatolian and Eastern Anatolian faults) might accommodate most of the western motion of the Anatolian block as it is compressed during convergence (Jackson and McKenzie, 1984). At a large scale, the Van region sits at the tip of a westward extruding wedge. Relatively complete earthquake records (Utkucu, 2013) for the Van region suggest several destructive events hit this area since 1500 AD, with at least 40 events (M>5) identified (Utkucu, 2013). For example, e.g. the 1670 Mus-Bitlis earthquake extended from Lake Van in a W-SW direction and a M_S 7.3 strike-slip earthquake in 1976 was 90 km northeast of the 2011 Van event (Stewart and Kanamori, 1982). These events within the triple junction zone of the Anatolian, Eurasian and Arabian plates (Chorowicz et al., 1994) reflect its complex geological background. However, the 1715 earthquake is the only reported destructive event in the Bardakçı-Saray thrust fault zone. For this reason, the fault zone did not appear in existing active fault maps (Utkucu, 2013). Along with several large aftershocks, this event led to over 600 people being killed and more than 60,000 made homeless.

Several papers have investigated the coseismic deformation, focal mechanisms and aftershocks of this event (Altiner et al., 2013; Elliott et al., 2013; Fielding et al., 2013; Irmak et al., 2012; Moro et al., 2014; Utkucu, 2013; Zahradník and Sokos, 2014). The mechanisms of the mainshock determined from geodetic observations and seismic waveforms are generally consistent. However, both the magnitudes and patterns of slip vary between models. For example, two-equal-sized areas of slip each with

maximum slip of ~9 m were calculated from InSAR observations by Elliott *et al.* (2013), whilst another study that combined InSAR with a SAR pixel offset map and GPS data suggested only one slip patch with a maximum slip of ~ 4 m (Fielding et al., 2013). This discrepancy has not yet to be resolved.

This paper will: (1) investigate the postseismic motion after the mainshock and assess its potential impacts on coseismic modelling; (2) differentiate coseismic and postseismic slip distributions using carefully selected geodetic data; (3) explore the effects of applying a layered Earth crustal model and discuss the correlation between coseismic slip and topography; and, (4) consider the mechanical implications of the relative spatial distributions of coseismic and postseismic slips.

2. Geodetic observations and modelling

2.1 Data sources

Three descending tracks of SAR observations (one track from COSMO-SkyMED (CSK), one track from Envisat ASAR, and one track from RADARSAT-2 (RS2)) were used in this study (Table 1). The slave CSK1 image was acquired on 23rd October 2013, just 4 h after the main shock and is considered to exclude any post-seismic motion. The slave ASAR image was acquired 8 days later (31st October 2011) so there should be a postseismic component within its phase measurements. Combining the coseismic CSK1 observations with this ASAR interferogram is ideal for assessing the impacts of postseismic signals on coseismic modelling. In this paper, two independent interferometric pairs are selected to investigate postseismic motion after the large event: one CSK pair spanning the first 4 days after the main shock, and one RS2 pair covering the subsequent 51 days (Table 1).

Eleven GPS coseismic measurements from a previous study (Altiner et al., 2013) are used for model validation. Using 1-second continuous GPS recording from the CORS-TR network, coseismic displacements were determined in the Precise Point Positioning mode with the Bernese GNSS software (Altiner et al., 2013). The maximum horizontal coseismic displacements of -16.95 mm in E-W direction and -34.2 mm in the N-S direction were found at the MURA GPS station, approximately 60 km northeast of the epicentre.

2.2 Coseismic interferograms

The CSK and ASAR interferograms were generated using the JPL/Caltech ROI_PAC V3.1Beta (Rosen et al., 2004) package (Table 1), whilst GAMMA software

(Wegmüller and Werner, 1997) was employed to produce RS2 interferograms. The topographic phase contribution was removed using a version of the Shuttle Radar Topography Mission (SRTM) 3 arc-second (~90 m) digital elevation model (DEM) (Farr et al., 2007) that has the voids filled from other data sources (Jarvis et al., 2008). The DEM had also been transformed into an ellipsoidal height datum (Li et al., 2013). The interferograms were unwrapped using the SNAPHU algorithm (Chen and Zebker, 2000) to obtain line-of-sight (LOS) displacements with Goldstein filtering (Goldstein and Werner, 1998).

Along-track interferometry was implemented to generate an along-track (azimuth) interferogram for the CSK pair of 20111010-20111023 using the open-source codes developed by Barbot *et al*. (2008). A precision of 0.1 m can be obtained when a bandpass filter is applied to an already focused SLC image to separate it into forward- and backward-looking scenes (Barbot et al., 2008; Bechor and Zebker, 2006; Feng et al., 2013; Hu et al., 2012). Note that along-track InSAR phase is not sensitive to SAR orbital errors, in the way that along-track pixel offsets are. Additionally, some across-track stripes can be observed in the original CSK azimuth interferogram (Figure S1(a)). These regular signals should not result from the coseismic rupture, which have been largely suppressed by applying a band-cut filter (Kobayashi et al., 2009) (Figures S1(b) and 2(b)). A southward movement can be clearly observed in the NW part of Figure 2(b), suggesting that the event occurred on a NW-dipping thrust fault which is consistent with the azimuth subpixel offset map in a previous study (Fielding et al., 2013).

2.3 Postseismic motion

Two independent pairs of SAR images collected after the main shock were analysed to investigate postseismic motion: the CSK2 pair from 4 h to three days after the mainshock and the RS2 pair spanning 48 days from the fourth day after the mainshock (Table 1). In Profiles A-A', B-B', E-E' and F-F', uplift signals of up to 0.06 m can be observed near the fault trace above 38.65 °N in the CSK2 interferogram, which are believed to be due to aftershocks (Elliott et al., 2013). Subsidence signals can also be seen in all the six CSK2 profiles, and similar signals appear in Profiles B-B', C-C' and D-D' in the RS2 interferogram covering a 48 days interval after the 23 October 2011 mainshock, suggesting that these signals are surface movements and not generated by atmospheric effects. These results also indicate that the ASAR coseismic interferogram using a second image acquired eight days after the main shock will also contain postseismic signals.

2.4 Coseismic modelling

To avoid possible spatial correlation of pixels and to accelerate modelling, interferograms were downsampled to create more manageable data sets with a data resolution-based (Rb) decomposition algorithm (Lohman and Simons, 2005). 1104 and 1375 points were extracted from the conventional and azimuth CSK interferograms (Figure S2 (a,b)), respectively. Azimuth displacements were weighted with a relative factor of 0.15 to LOS range changes based on the residuals after subtracting the best-fitted model with an equal weight, and all data points in each dataset were equally weighted.

Based on field survey (Doğan and Karakaş, 2013), the 2011 Van earthquake was recognized as a blind faulting event that did not break the surface. There is insufficient evidence to determine if the rupture occurred over a non-planar surface. Therefore, for simplicity, a single fault plane was used to characterize this earthquake. A two-step inversion strategy was employed to determine its source parameters and variable slip distribution which comprises a nonlinear inversion for determining the fault geometry, and a linear inversion for estimating the slip distribution along the ruptured fault plane. The elastic half-space dislocation model (Okada, 1985) was used for generating a Green's matrix.

In Step 1, the weighted best-fit function ε was designed to determine the optimal geometric parameters using,

$$\varepsilon = \sqrt{(W(D - GS))^2 / N} \quad (1)$$

where G is the design matrix for the surface response of 1 m slip over the uniform rectangular fault in the radar line of sight (LOS) with a unit length and width for both strike and dip components, S is the slip vector, W is the relative weight for each dataset, D are downsampled coseismic observations and N is the number of observations used in the inversion. The best-fit uniform model suggests that the earthquake occurred on a NNW dipping fault with a strike of 261.3° and a dip of 47.3° (Table 2).

In Step 2, using the fault geometry determined in Step 1, the fault plane was extended along strike and downdip by increasing its total length to 40 km and downdip width to 40 km, and then divided into 400 sub-faults each measuring 2 km by 2 km. The best

fit values of strike-slip and dip-slip motion for each sub-fault were solved using a non-negative least squares algorithm (Ward and Barrientos, 1986). Meanwhile, a Laplacian smoothing constraint was employed to prevent physically impossible oscillatory slip (Harris and Segall, 1987). In the linear inversion step, the basic inverse problem was expressed by

$$\begin{bmatrix} G \\ \alpha^2 L \end{bmatrix} S = \begin{bmatrix} D \\ 0 \end{bmatrix} \quad (2)$$

where L is an order-2 differential operator defined by Harris and Segall (1987) for a roughness estimate and α^2 is the controlling parameter. Since the fault dip angle obtained from the uniform inversion (Step 1) may differ slightly from the global optimal parameters for slip distribution (Burgmann et al., 2002; Fukahata and Wright, 2008), an iterative approach was implemented to estimate the optimal dip angle in the slip inversion (Feng et al., 2013).

Our optimal slip model with CSK LOS range changes and azimuth displacements suggests that the maximum slip of 6.5 m occurred at a depth of 12 km with a purely reverse slip (Figure 4(a)). The major slip area is concentrated between 8 and 25 km. Slip of >3 m is found at shallower depths with a secondary maximum at 10km depth SW of the epicentre, up to ~ 10 km away from the maximum slip location (Figure 4(a)). This two-patch slip distribution is supported by a two-point source solution (Zahradník and Sokos, 2014) and the seismic rupture solution in Fielding *et al*. (2013). The released moment from the variable slip model reaches up to $4.19{+}10^{19}$ N.m, approximately equivalent to a moment magnitude of M_W 7.03. Figure 5 shows CSK observations, simulated interferograms from the optimal slip distribution, and their residuals. The best-fit slip distribution agrees well with CSK observed displacements with small root mean square (RMS) misfits: 0.015 m to CSK LOS range changes, 0.070 m to CSK azimuth displacements.

To determine errors for the optimal slip distribution, a Monte Carlo simulation of correlated noise was used (Funning et al., 2005; Li et al., 2008; Parsons et al., 2006; Wright et al., 2003). A 1-D covariance function was estimated using the residual interferogram. Using a variance- covariance matrix for the sampled data points, 100 sets of correlated noise were simulated to create 100 perturbed data sets. The linear inversion procedure was applied to each of these data sets and the distribution of best fitting solutions provides information on slip errors (Figure S3). The largest uncertainties in the dip-slip, < 0.8 m, are at 20 km depth (Figure S3(d)), which is an order or magnitude smaller than the optimal slip (Figure S3(a)). The uncertainties in

the strike slip near the surface (Figure S3(c)) might be due to the differences between our simplified fault plane model and the slightly curved and stepped geometry of the real fault trace. The average slip uncertainty is less than 0.25 m, providing confidence about the overall slip distribution.

The ASAR coseismic interferogram covers the period from 5th November 2010 to 31st October 2011, so it includes postseismic motion within the first 8 days after the mainshock. To examine the impacts of including postseismic signals on coseismic modelling, 1597 datapoints (Figure S2(d)) were extracted from the ASAR interferogram using the data resolution-based resampling method as used for CSK data. Equal weights were applied in modelling for both ASAR and CSK1 LOS range changes, as in previous studies (Elliott et al., 2013). Figure 4(c) shows the resultant best-fit slip distribution. This overall slip pattern is generally consistent with the model constrained only using CSK data (Figure 4(a)), but the maximum slip is more than 1 m lower in the joint inversion. This difference is most likely to be due to postseismic movement affecting the ASAR phase measurements. Therefore, Model A derived from CSK1 LOS range changes and azimuth offsets is the preferred model of the coseismic slip distribution in this study.

2.5 Postseismic Modelling

The only available CSK2 interferogram covering the period from 4 h to 3 days after the mainshock was used to determine the initial postseismic behaviour following the main shock. Several physical mechanisms can contribute to postseismic deformation (Fialko, 2004; Ryder et al., 2007), including afterslip, poroelastic rebound and viscoelastic relaxation. Following Peltzer *et al*'s approach (1998) different Poisson's ratios were used for undrained and drained upper crust conditions to simulate potential surface deformation caused by poroelastic relaxation . This Modelling produced a pattern of uplift which is opposite to that observed from the postseismic interferograms in this study. Thus, fluid flow in the porous media can be ruled out as a postseismic deformation mechanism. Viscoelastic relaxation induced deformation in the CSK2 observations should also be limited since this interferogram covers only the first 3 days which is insufficient time to generate significant surface movements given that the viscosity of lower crust in this region could reach up to 10^{22} Pa.s (Riva and Govers, 2009). Therefore, only afterslip is considered to be a significant contribution to postseismic deformation.

The same optimal fault geometry and fault discretization that were determined in the

coseismic modelling were applied in postseismic modelling. 558 points were extracted by the data R-based downsampling method (Figure S2(c)) . The same distributed slip inversion strategy as described above was applied to determine a best-fit afterslip model. As shown in Figure 9, the postseismic slip is concentrated in the zone directly above the locus of coseismic rupture, has a maximum slip of 1.5 m, and approaches but does not break the surface. The accumulative moment release is up to $1.5+10^{19}$ N.m, which is equivalent to a magnitude 6.7. As shown in Figure 3, predicted CSK LOS changes (gray points) are in good agreement with observations (the red ones) with an average correlation coefficient of 0.86.

3 Discussion

3.1 Effects of Layered Earth Model on the Variable Slip Model

The localized crustal structure in the vicinity of the epicentre from the Crust 2.0 database shows some stratification , particularly in the upper 20 km where the major coseismic rupture occurred. Wang *et al.* (2010) suggested that effects of a layered earth model might be significant in some cases of coseismic modelling, therefore a numerical experiment with a layered model was performed. The package PSGRN/PSCMP developed by Wang *et al*. (2006) was employed to generate the unit slip surface response in the data inversion. As presented in Figure 4(e), the best-fit model suggests that the maximum slip and distributed patterns are consistent with those from the elastic half-space Model A, both having RMS of 5 mm for InSAR observations. The average rake angle of the patches with slip > 1.5 m is ~79°, which is closer to the seismic solution (Irmak et al., 2012) relative to an average rake angle of 86° determined from the elastic half-space model.

An independent examination was also performed using regional GPS coseismic measurements (Figure 7). The RMS of 3.9 mm for horizontal components from Model A drops to 2.6 mm for those from Model E, while the RMS of 5.0 mm for vertical components drops to 4.9 mm for Model E. The correlation between simulated and observed horizontal components exceeds 0.96 for Model E, against 0.86 for Model A. There is a discrepancy between GPS measurements from (Altiner et al., 2013) and those posted on the Geohazard Supersite (http://supersites.earthobservations.org/van.php), possibly due to different strategies used in GPS data processing. For instance, Altiner *et al* (2013) give a south-north displacement at the MURA station of ~34.02 mm (Altiner et al., 2013), whilst the GEO-Supersite provides a value of 54.5±3 mm . The vertical components have large uncertainties (Altiner et al., 2013) and are not suitable for verifying slip models.

However, the high consistency between Altiner *et al*'s GPS horizontal components and those simulated by Model E suggests that the layered slip model is preferable in this event. The major differences between Models A and E mainly come from the shallow part (less than 6 km), where there is the largest uncertainty in determining slip (Figure S(3)).

3.2 Comparisons with published slip distributions

There have been several seismic solutions published for the 2011 Van earthquake (Ashtari Jafari, 2013; Fielding et al., 2013; Irmak et al., 2012; Utkucu, 2013; Zahradnik and Sokos, 2013), most suggesting that the major rupture propagated along the dip direction from its origin to 10 seconds with a maximum slip of ~4 m near the epicentre, and another small amount of energy was released from 10-18 seconds (Fielding et al., 2013; Irmak et al., 2012). The entire rupture lasted for less than 20 seconds. The principal planes with strike ranging from 241° to 281°, dip from 38° to 71° and rake from 59° to 71° were determined through the focal moment inversion. Although the depth of the maximum slip varies in the published slip models, the major slip patch is observed with a maximum magnitude of ~ 4 m in the deeper part followed by a small shallow event in the seismic waveform inversions (Fielding et al., 2013; Irmak et al., 2012), which is also supported by two-point source modelling (Zahradník and Sokos, 2014).

Two geodetic models have also been published for this large event (Elliott et al., 2013; Fielding et al., 2013), both suggesting the maximum slip occurred at a depth of 12-14 km, but with different slip magnitudes and patterns. A complicated slip model with two-equal-size slip patches with a maximum of ~9 m at a depth of 12-14 km for both patches was determined by Elliott *et al.* (2013), which may relate with the employed geometric model and inversion method. A single-patch slip distribution with a maximum slip of ~ 4 m at a depth of 12 km by Fielding *et al*. (2013) using GPS and a different CSK pair together which includes significant postseismic observations, with identical ASAR pairs. It is notable that: (1) two identical ASAR pairs were used in both studies for coseismic modelling; (2) Elliott *et al.* (2013) used a CSK coseismic pair with the second image acquired just 4 h after the main shock, whilst Fielding *et al.* (2013) used one with a CSK image acquired 3 days later; and, (3) Fielding *et al*. (2013) included CSK azimuth offsets and GPS released by JPL in their modelling.

To minimize the impacts of postseismic signals, ASAR pairs were excluded and only InSAR observations and along-track (azimuth) displacements from the CSK pair that

minimises post-seismic motions were used in our coseismic modelling (Table 1; Section 2.4). Note that both the beam splitting technique in this study and the SAR offset technique used by (Fielding et al., 2013) provide horizontal displacements in the satellite azimuth direction (along-track), and the former appears to provide observations with a better precision (~0.08 m for beam splitting, ~0.12 m for azimuth offsets) (Bechor and Zebker, 2006; Feng et al., 2013; Jung et al., 2009). The maximum slip of 6.5 m at a depth of 12 km is observed in our preferred coseismic model. Additionally, a second shallow slip patch is seen at the southwest of the fault plane, which is similar to another two published seismic models [e.g. Irmak *et al*. 2012; Fielding et al., 2013] although it does not appear in the two published InSAR models (Elliott et al., 2013; Fielding et al., 2013). As mentioned in Section 2.4, a simplified fault plane was assumed in the coseismic modelling by neglecting the slightly curved and stepped geometry of the fault trace. Figure 4 shows that the major slip all occurred at the depth of at least 8 km, implying that the impact of this assumption of a simplified fault plane should be limited. On the basis of independent GPS data, the performance of the single slip model in this study is an improvement on that of the two-fault model determined by Elliott *et al*. (2013). Altiner *et al.* (2013) also gave a simple single-fault slip solution with a maximum slip of 4 m under the constraints of limited far-field GPS measurements. Because GPS observations are too distant from the fault and sparse to accurately determine the fault location and slip pattern, their slip model was not compared here.

3.3 Correlation between coseismic slip and topography

Two coseismic slip patches have been revealed through inverting the CSK coseismic observations in section 2.4. One ranges from 0-15 km along the strike direction with a maximum slip of 6.5 m at a depth of 12 km, the other ranges from 15 to 22 km along the strike direction with a maximum slip of 2.5 m at a depth of 8 km. The projected slip on the surface (Figure 8) is correlated with the surface topography, cosesimic rupture extending through the low elevation area.

The role of subducted seamounts in the nucleation and rupture propagation of large subduction earthquakes have been widely discussed (Bilek et al., 2003; Das and Watts, 2009; Dixon and Moore, 2007; Hicks et al., 2012; Schurr et al., 2012; Yang et al., 2013a). A series of earthquakes between 1983 to 1999 along the Costa Rican subduction zone led to the suggestion that spaced isolated seamounts could act as asperities (Bilek et al., 2003). Recent investigation of the 2010 Mule, Chile earthquake (Hicks et al., 2012) also suggested that the subducted structure can be conductive to the nucleation of the earthquake, and can also hinder coseismic slip and

aftershock activities. The latter suggestion is consistent with the conclusions drawn from numerical experiments by Yang *et al*. (2013a).

To examine whether similar features can be found in the 2011 Van event, an intraplate large thrust earthquake, the relative shear stress exerted on the fault plane by the overlying topography was calculated. At a given depth, the relative gravity resistance along the inclined fault can be derived from $\sigma = \tau_t + \theta\sigma_t^n$, here τ_t and σ_t^n are the relative gravity ($\Delta G = \rho g \Delta h$) induced shear stress and normal stress on the plane, which can be determined using a trigonometric function of the fault dip angle. θ is a frictional coefficient (>0) and pore pressure is ignored. These calculation produce relative resistance ranging from 4-14 MPa along the fault plane as shown in Figure 8(b). Note that the major aim here is to identify the potential locations of subducted mounts along the fault plane qualitatively, rather than quantitative stress analysis from topography. This pattern of stress suggests that the 2011 Van earthquake starts in the zone with relative high resistance and extends towards the area of low resistance, which implies that topography might be one factor influencing nucleation of a large intraplate thrust earthquake as well as the magnitude of rupture.

3.4 Mechanical implications of the slip models

Large earthquakes can permanently alter ambient stress level and trigger seismicity over a large area (King et al., 1994). Particularly, slip on blind thrust faults can significantly increase stress above the source fault and in other nearby zones (Lin and Stein, 2004). Driven by the coseismic stress, a fault may creep aseismically (Barbot et al., 2009). Stress-driven creep has already been observed during postseismic and interseismic phases of earthquake cycles along different active fault systems (Barbot et al., 2009; Freed et al., 2006; Hetland and Simons, 2010; Johnson and Fukuda, 2010; Johnson and Segall, 2004; Wang et al., 2012). Therefore, better understanding of the mechanical properties within a fault system will improve seismic risk assessment following a large earthquake.

In this study, the shear stress along the fault plane was calculated by three-dimensional elastic dislocation model (Okada, 1992). The largest shear stress drop located in the earthquake zone reaches up to -12 MPa (decreased) (Figure 9 (a)), which is compatible with the stress drop of 17 MPa during the 2010 M_W 8.8 earthquake (Luttrell et al., 2011). The upward shear stress increases along the fault plane and reaches a maximum of 5 MPa that is also nearly equivalent in magnitude with the Mule earthquake. It's clear in Figure 9(a) that the zone of the greatest shear

stress increase overlies the region of maximum afterslip. Since only one M_W 5.6 aftershock was recorded during the period from 4 h to three days after the mainshock, most of the postseismic moments revealed by the CSK2 interferogram are considered to be released by aseismic creep.

Significant afterslip is concentrated in a small region that has a relative high resistance exerted by topography (Figure 9(b)). This is consistent with the previous suggestion that subducted mounts can be favourable location for accumulating interseismic strain energy and where the failure threshold can be reached due to the effects of perturbed cosesimic stress. Because no further postseismic observation covering the initial period is available, the slip model remains uncertain. However, the RS2 postseismic interferogram which covers 4-52 days after the mainshock also shows similar pattern, implying the observations used in this study should reflect the real postseismic behaviour .

Additionally, postseismic slip has an average rake angle of 30° for those slip patches with > 0.5 m slip, which is significantly different from the value of ~80° (nearly pure dipping) determined for coseismic slip. This difference may suggest that large coseismic rupture significantly decreased stress in the vicinity of the earthquake rupture zone. For a thrust earthquake, the three principal stresses should be in the sequence $\sigma_1 > \sigma_2 > \sigma_3$, where the greatest stress σ_1 and intermediate stress σ_2 plunge horizontally, and the minimum principal stress σ_3 is vertical (Zoback et al., 1989). Although stress inversion from a slip model on one straight fault plane is limited as regional stress cannot be constrained from a single fault (McKenzie, 1969), a qualitative analysis still can offer a chance to explore how coseismic processes affect the variation of the regional stress. The pattern of oblique afterslip with a mean rake angle of 30° implies the P-axes trending NE-SW along 33°, whilst P-axes determined from coseismic slip trends nearly N-S along 354°. Observation errors cannot account for the ~30° difference between these directions. The difference in orientations may indicate that the stress in the earthquake zone was decreased to a low level during the coseismic rupture, which is consistent with one seismicity analysis for this event (Görgün, 2013). If the focal mechanisms of a number of earthquakes before the mainshock can be collected, it would be possible to estimate deviatoric stress in the earthquake zone, as has been done for the 2011 Tohoku-Oki, Japan earthquake (Yang et al., 2013b). However, this analysis is far beyond what is possible using only InSAR-determined slip models.

4 Conclusions

In this paper, multi-source SAR images were used to investigate coseismic displacements of the 2011 Van (Turkey) earthquake, and rapid postseismic signals were observed even in the interferograms covering 3-day and 48-day periods after the main shock. Our modelling suggests that use of interferograms with obvious postseismic signals can lead to a reduction of about 1 m in the calculated magnitude of the slip distribution, although with a similar slip pattern. Therefore, reliable coseismic slip modelling requires interferograms from data acquired after the event. The availability of such data will improve as more SAR missions with smaller repeat cycles are made available in the very near future.

Our preferred coseismic slip model with a careful selection of SAR observations (i.e. CSK1 interferogram and azimuth displacements, Table 1 and Figure 2) suggests: (1) this large event occurred on a north-west dipping thrust fault with a strike of 261º and dip of 49º; (2) a maximum slip of 6.5 m is observed at a depth of ~12 km; (3) a shallow asperity has been identified in the southwest of the major slip zone; and, (4) the released moment is equivalent to a magnitude of M_W 7.03.

The afterslip is also revealed by the second CSK interferogram which covers the first three days after the main shock. Our optimal afterslip model suggests that a maximum slip of 1.5 m occurred at a depth of 5 km, located directly above the locus of coseismic rupture. The accumulated moment in the first three postseismic days reached up to $1.5+10^{19}$ N.m. The accumulative moment release cannot be accounted for from the recorded aftershocks, suggesting most of the postseismic moment is released by aseismic creep. An obvious variation in the slip vectors between coseismic and postseismic motion has been identified, which may imply a significant rotation of the axis of greatest principal stress. As also found in the 1994 Northridge, California earthquake (Donnellan et al., 2002), rapid afterslip may commonly happen after an large earthquake, especially in thrust events.

Acknowledgements

WF is supported by a China Scholarship Council (CSC) scholarship and the University of Glasgow. The work was part-supported by: the UK Natural Environment Research Council (NERC) through the National Centre for Earth Observation (NCEO), of which the Centre for the Observation and Modelling of Earthquakes, Volcanoes and Tectonics (COMET) is part; and, the National Science Foundation of China (Project ID: 41104028). We are very grateful to Dr John Elliott for sharing CSK data, and to

Andrew Singleton for useful discussions. RADARSAT-2 data was provided by the Canadian Space Agency. All figures were prepared in the paper with GMT software (Wessel and Smith, 1998) .

References

Aksoy, E., Türkmen, İ., Turan, M., 2005. Tectonics and sedimentation in convergent margin basins: an example from the Tertiary Elazığ basin, Eastern Turkey. Journal of Asian Earth Sciences 25, 459-472. doi:http://dx.doi.org/10.1016/j.jseaes.2004.04.009.

Altiner, Y., Söhne, W., Güney, C., et al., 2013. A geodetic study of the 23 October 2011 Van, Turkey earthquake. Tectonophysics 588, 118-134. doi:http://dx.doi.org/10.1016/j.tecto.2012.12.005.

Ashtari Jafari, M., 2013. Combination of double couple and non-double couple events during the Van, Turkey, 2011 earthquake sequence. Journal of Asian Earth Sciences 67–68, 63-75. doi:http://dx.doi.org/10.1016/j.jseaes.2013.01.025.

Barbot, S., Fialko, Y., Bock, Y., 2009. Postseismic deformation due to the Mw6.0 2004 Parkfield earthquake: Stress-driven creep on a fault with spatially variable rate-and-state friction parameters. J. Geophys. Res. 114. doi:10.1029/2008JB005748.

Barbot, S., Hamiel, Y., Fialko, Y., 2008. Space geodetic investigation of the coseismic and postseismic deformation due to the 2003 MW7.2 Altai earthquake: Implications for the local lithospheric rhecology. J. geophys. Res 113. doi:10.1029/2007JB005063.

Bechor, N.B.D., Zebker, H.A., 2006. Measuring two-dimensional movements using a single InSAR pair. Geophys. Res. Lett. 33, L16311. doi:10.1029/2006GL026883.

Bilek, S.L., Schwartz, S.Y., DeShon, H.R., 2003. Control of seafloor roughness on earthquake rupture behavior. Geology 31, 455-458. doi:10.1130/0091-7613(2003)031<0455:cosroe>2.0.co;2.

Burgmann, R., Ayhan, M.E., Fielding, E.J., et al., 2002. Deformation during the 12 November 1999 Duzce, Turkey, earthquake, from GPS and InSAR data. Bulletin of the Seismological Society of America 92, 161-171.

Chen, C.W., Zebker, H.A., 2000. Network approaches to two-dimensional phase unwrapping: intractability and two new algorithms. Journal of the Optical Society of America A 17, 401-414

Chorowicz, J., Luxey, P., Lyberis, N., et al., 1994. The Maras Triple Junction (southern Turkey) based on digital elevation model and satellite imagery interpretation. Journal of Geophysical Research: Solid Earth 99, 20225-20242. doi:10.1029/94jb00321.

Das, S., Watts, A.B., 2009. Effect of Subducting Seafloor Topography on the Rupture Characteristics of Great Subduction Zone Earthquakes, in: Lallemand, S., Funiciello, F. (Eds.), Subduction Zone Geodynamics. Springer Berlin Heidelberg, pp. 103-118.

Dewey, J.F., Pindell, J.L., 1985. Neogene block tectonics of eastern Turkey and northern South America: Continental applications of the finite difference method. Tectonics 4, 71-83. doi:10.1029/TC004i001p00071.

Dixon, T.H., Moore, J.C., 2007. The Seismogenic Zone of Subduction Thrust Faults. Columbia University Press.

Doğan, B., Karakaş, A., 2013. Geometry of co-seismic surface ruptures and tectonic meaning of the 23 October 2011 Mw 7.1 Van earthquake (East Anatolian Region, Turkey). Journal of Structural Geology 46, 99-114. doi:http://dx.doi.org/10.1016/j.jsg.2012.10.001.

Donnellan, A., Parker, J.W., Peltzer, G., 2002. Combined GPS and InSAR Models of Postseismic Deformation from the Northridge Earthquake. Pure and Applied Geophysics 159, 2261-2270.

doi:10.1007/s00024-002-8734-7.
Elliott, J.R., Copley, A.C., Holley, R., et al., 2013. The 2011 Mw 7.1 Van (Eastern Turkey) earthquake. Journal of Geophysical Research: Solid Earth 118, 1-19. doi:10.1002/jgrb.50117.
Farr, T.G., Caro, E., Crippen, R., et al., 2007. The Shuttle Radar Topography Mission. Reviews of Geophysics 45. doi:1029/2005RG000183.
Feng, W., Li, Z., John, E., et al., 2013. The 2011 Mw 6.8 Burma earthquake: fault constraints provided by multiple SAR techniques. Geophysical Journal International. doi:10.1093/gji/ggt254.
Fialko, Y., 2004. Evidence of fluid-filled upper crust from observations of post-seismic deformation due to the 1992 M_W7.3 Landers earthquake. J. Geophys. Res. 109. doi:10.1029/2004JB002985.
Fielding, E.J., Lundgren, P.R., Taymaz, T., et al., 2013. Fault-slip Source Models for the 2011 M 7.1 Van Earthquake in Turkey from SAR interferometry, Pixel Offset Tracking, GPS and Seismic Waveform Analysis. Seismological Research Letters 84. doi:10.1785/0220120164.
Freed, A.M., Bürgmann, R., Calais, E., et al., 2006. Implications of deformation following the 2002 Denali, Alaska, earthquake for postseismic relaxation processes and lithospheric rheology. Journal of Geophysical Research: Solid Earth 111, B01401. doi:10.1029/2005jb003894.
Fukahata, Y., Wright, T.J., 2008. A non-linear geodetic data inversion using ABIC for slip distribution on a fault with an unknown dip angle. Geophys. J. Int. 173, 353-364. doi:10.1111/j.1365-246X.2007.03713.x.
Funning, G.J., Parsons, B., Wrigth, T.J., 2005. Surface displacements and source paramenters of the 2003 Bam (Iran) earthquake from Envisat advanced synthetic aperture radar imagery. J. Geophys. Res. 110. doi:10.1029/2004JB003338.
Goldstein, R.M., Werner, C.L., 1998. Radar interferogram filtering for geophysical applications. Geophysical Research Letters 25, 4035-4038. doi:10.1029/1998gl900033.
Görgün, E., 2013. The 2011 October 23 Mw 7.2 Van-Erciş, Turkey, earthquake and its aftershocks. Geophysical Journal International. doi:10.1093/gji/ggt264.
Harris, R.A., Segall, P., 1987. Detection of a Locked Zone at Depth on the Parkfield, California, Segment of the San Andreas Fault. J. geophys. Res 92, 7945-7962.
Hetland, E.A., Simons, M., 2010. Post-seismic and interseismic fault creep II: transient creep and interseismic stress shadows on megathrusts. Geophys. J. Int. 181, 99-112. doi:10.1111/j.1365-246X.2009.04482.x.
Hicks, S.P., Rietbrock, A., Haberland, C.A., et al., 2012. The 2010 Mw 8.8 Maule, Chile earthquake: Nucleation and rupture propagation controlled by a subducted topographic high. Geophys. Res. Lett. 39, L19308. doi:10.1029/2012gl053184.
Hu, J., Li, Z., Zhang, L., et al., 2012. Correcting ionospheric effects and monitoring two-dimensional displacement fields with multiple-aperture InSAR technology with application to the Yushu earthquake. Sci. China Earth Sci. 55, 1961-1971. doi:10.1007/s11430-012-4509-x.
Irmak, T.S., Dogan, D., Karakas, A., 2012. Source mechanism of the 23 October, 2011, Van(Turkey) earthquake (Mw=7.1) and aftershocks with its tectonic implications. Earth Planets Space 64, 991-1003.
Jackson, J., McKenzie, D., 1984. Active tectonics of the Alpine–Himalayan Belt between western Turkey and Pakistan. Geophysical Journal of the Royal Astronomical Society 77, 185-264. doi:10.1111/j.1365-246X.1984.tb01931.x.
Jarvis, A., Reuter, H.I., Nelson, A., et al., 2008. Hole-filled seamless SRTM data V4. http://srtm.csi.cgiar.org.
Johnson, K.M., Fukuda, J.i., 2010. New method for estimation the spatial distribution of locked

asperities and stress-driven interseismic creep on faults with application to the San Francisco Bay Area, California. J. Geophys. Res. 115. doi:10.1029/2010JB007703.
Johnson, K.M., Segall, P., 2004. Viscoelastic earthquake cycle models with deep stress-driven creep along the San Andreas fault system. J. Geophys. Res 109. doi:10.1029/2004JB003096.
Jung, H.-S., Won, J.-S., Kim, S.-W., 2009. An Improvement of the Performance of Multiple-Aperture SAR Interferometry (MAI). IEEE Transactions on Geoscience and Remote Sensing 47, 2859-2869.
King, G.C.P., Stein, R.S., Lin, J., 1994. Static Stress Changes and the Triggering of Earthquakes. Bull. Seism. Soc. Am. 84, 935-953.
Kobayashi, T., Takada, Y., Furuya, M., et al., 2009. Locations and types of ruptures invoved in the 2008 Sichuan earthquake inferred SAR image matching. Geophys. Res. Lett. 36. doi:10.1029/2008GL036907.
Li, P., Li, Z., Shi, C., et al., 2013. Impacts of geoid height on large-scale crustal deformation mapping with InSAR observations. Chinese J. Geophys. (in Chinese) 56, 1857-1867. doi:10.6038/cjg20130608.
Li, Z., Feng, W., Xu, Z., et al., 2008. The 1998 Mw5.7 Zhangbei-Shangyi (China) earthquake revisited: A buried thrust fault revealed with interferomertic synthetic aperture radar. Geochem. geophys. Geosyst. 9, Q04026. doi:10.1029/2007GC001910.
Lin, J., Stein, R.S., 2004. Stress triggering in thrust and subduction earthquakes and stress interaction between the southern San Andreas and nearby thrust and strike-slip faults. J. Geophys. Res. 109, B02303. doi:10.1029/2003JB002607.
Lohman, R.B., Simons, M., 2005. Some thoughts on the use of InSAR data to constrain models of surface deformation: Noise structure and data downsampling. Geochemistry, Geophysics, Geosystems 6, Q01007. doi:10.1029/2004gc000841.
Luttrell, K.M., Tong, X., Sandwell, D.T., et al., 2011. Estimates of stress drop and crustal tectonics stress from the 27 February 2010 Maule, Chile, earthquake: Implications for fault strength. J. Geophys. Res. 116. doi:10.1029/2011JB008509.
McKenzie, D.P., 1969. The relation between fault plane solutions for earthquakes and the directions of the principal stresses. Bulletin of the Seismological Society of America 59, 591-601.
Moro, M., Cannelli, V., Chini, M., et al., 2014. The October 23, 2011, Van (Turkey) earthquake and its relationship with neighbouring structures. Sci. Rep. 4. doi:10.1038/srep03959
http://www.nature.com/srep/2014/140210/srep03959/abs/srep03959.html#supplementary-information.
Okada, Y., 1985. Surface Deformation Due to Shear and tensile faults in a half-space. Bull. Seism. Soc. Am. 75, 1135-1154.
Okada, Y., 1992. Internal deformation due to shear and tensile faults in a half-space. Bull. Seism. Soc. Am. 85, 1018-1040.
Parsons, B.E., Wright, T.J., Powe, P., et al., 2006. The 1994 Sefidabeh (eastern Iran) earthquakes revisited: new evidence from satellite radar interferometry and carbonate dating about the growth of an active fold above a blind thrust fault. Geophys. J. Int. 164, 202~217.
Peltzer, G., Rosen, P., Rogez, F., 1998. Poroelastic rebound along the Landers 1992 earthquake surface rupture. J. Geophys. Res. 103, 30131-30145.
Relinger, R., McClusky, S., Vernant, P., et al., 2006. GPS constraints on continental deformation in the Africa-Arabia-Eurasia continental collision zone and implications for the dynamics of plate interactions. J. Geophys. Res. 111. doi:10.1029/2005JB004051.
Riva, R.E.M., Govers, R., 2009. Relating viscosities from postseismic relaxation to a realistic viscosity structure for the lithosphere. Geophysical Journal International 176, 614-624.

doi:10.1111/j.1365-246X.2008.04004.x.
Rosen, P.A., Henley, S., Peltzer, G., et al., 2004. Updated Repeat Orbit Interferometry Package Released. EOS, Transactions American Geophyical Union 85. doi:10.1029/2004EO050004.
Ryder, I., Parsons, B., Wright, T.J., et al., 2007. Post-seismic motion following the 1997 Manyi (Tibet) earthquake: InSAR observations and modelling. Geophys. J. Int. 169, 1009-1027. doi:10.1111/j.1365-246X.2006.03312.x.
Schurr, B., Asch, G., Rosenau, M., et al., 2012. The 2007 M7.7 Tocopilla northern Chile earthquake sequence: Implications for along-strike and downdip rupture segmentation and megathrust frictional behavior. Journal of Geophysical Research: Solid Earth 117, B05305. doi:10.1029/2011jb009030.
Stewart, G.S., Kanamori, H., 1982. Complexity of rupture in large strike-slip earthquakes in Turkey. Physics of the Earth and Planetary Interiors 28, 70-84. doi:10.1016/0031-9201(82)90118-2.
USGS, 2011. Magnitude 7.1 - EASTERN TURKEY, in: http://earthquake.usgs.gov/earthquakes/eqinthenews/2011/usb0006bqc/ (Ed.).
Utkucu, M., 2013. 23 October 2011 Van, Eastern Anatolia, earthquake (Mw 7.1) and seismotectonics of Lake Van area. Journal of Seismology, 1-23. doi:10.1007/s10950-012-9354-z.
Wang, L., Hainzl, S., Zöller, G., et al., 2012. Stress- and aftershock-constrained joint inversions for coseismic and postseismic slip applied to the 2004 M6.0 Parkfield earthquake. Journal of Geophysical Research: Solid Earth 117, B07406. doi:10.1029/2011jb009017.
Wang, R., Lorenzo-Martin, F., Roth, F., 2006. PSGRN/PSCMP-a new code for calculating co- and post-seismic deformation, geoidf and gravity changes based on the viscoelastic-gravitational dislocation theory. Computers & Geosciences 32, 527-541.
Wang, W., Sun, W., Jiang, Z., 2010. Comparison of fault models of the 2008 Wenchuan earthquake (Ms8.0) and spatial distributions of co-seismic deformations. Tectonophysics 491, 85-95. doi:10.1016/j.tecto.2009.08.035.
Ward, S., Barrientos, S., 1986. An inversion for slip distribution and fault shape from geodetic observations of the 1983, Borah Peak, Idaho, earthquake. J. geophys. Res 91, 4909-4919.
Wegmüller, U., Werner, C., 1997. Gamma SAR processor and interferometry software. ESA SP, 1687-1692.
Wessel, P., Smith, W.H.F., 1998. New, improved version of generic mapping tools released. EOS, Transactions American Geophysical Union 79, 579-579. doi:10.1029/98eo00426.
Wright, T.J., Lu, Z., Wicks, C., 2003. Source model for the Mw6.7, 23 October 2002, Nenana Mountain Earthquake (Alaska) from InSAR. Geophys. Res. Lett. 30. doi:10.1029/2003GL018014.
Yang, H., Liu, Y., Lin, J., 2013a. Geometrical effects of a subducted seamount on stopping megathrust ruptures. Geophysical Research Letters, n/a-n/a. doi:10.1002/grl.50509.
Yang, Y.-R., Johnson, K.M., Chuang, R.Y., 2013b. Inversion for absolute deviatoric crustal stress using focal mechanisms and coseismic stress changes: The 2011 M9 Tohoku-oki, Japan, earthquake. Journal of Geophysical Research: Solid Earth 118, 2013JB010224. doi:10.1002/jgrb.50389.
Zahradnik, J., Sokos, E., 2013. the Mw7.1 Van, Eastern Turkey, earthquake 2011 - two-point source modeling by iterative doconvolution and nonnegtive least squares. Geohy. J. Int. (in review).
Zahradník, J., Sokos, E., 2014. The Mw 7.1 Van, Eastern Turkey, earthquake 2011: two-point source modelling by iterative deconvolution and non-negative least squares. Geophysical Journal International 196, 522-538. doi:10.1093/gji/ggt386.
Zoback, M.L., Zoback, M.D., Adams, J., et al., 1989. Global patterns of tectonic stress. Nature 341, 291-298.

Figure 1 (a) Tectonic background of the 2011 M_W 7.1 Van, Turkey earthquake overlaid with GPS velocities (Relinger et al., 2006). Red star is the epicentre of the 2011 earthquake (USGS, 2011). (b) Seismic activity in the Van region, The arrow shows the convergence rate revealed by GPS (Relinger et al., 2006). Dashed rectangles indicate the coverage of SAR images used in this study, yellow circles represent aftershocks (http://www.emsc-csem.org/, last accessed on 28 December 2012) and beach balls show the mechanisms of major aftershocks determined by Irmak *et al.* (2012). Background is DEM derived from the Shuttle Radar Topography Mission digital elevation model (Farr et al., 2007).

Figure 2. CSK pair spanning the period from 10th October 2011 to 13th October 2011: (a) Coseismic interferogram with LOS range changes being re-wrapped in the range of -0.05 to 0.05 m. (b) Along-track (azimuth) displacement from the spectrum splitting method (Barbot et al. 2008). Arrows represent horizontal surface movements in the along-track direction.

Figure 3 (a) CSK2 postseismic interferogram covering the period from 23rd October 2011 to 26th October 2011; (b) RS2 postseismic interferogram covering the period from 26th October 2011 to 13th December 2011. (c) Predicted CSK2 postseismic interferogram from the best-fit afterslip model. (d) the residuals between (a) and (c). Profiles A-A', B-B', C-C', D-D', E-E' and F-F' show postseismic (red dots for CSK2 and green triangles for RS2) and coseismic (blue diamonds) range changes in the LOS direction as well as topography variations (gray shadow). Note Profile locations are shown in (A) and (B), and red lines in (A) and (B) and black lines in all the profiles indicate the fault location.

Figure 4. (a) Model A: Slip distribution determined with CSK LOS range changes and azimuth offsets; (b) Released moment for Model A; (c) Model C: slip distribution determined with a combination of CSK and ASAR; (d) Released moment for Model C; (e) Model E: slip distribution with a layered earth model using the same constraints as Model A; (f) Released moment for Model E. Noted that an identical dip angle of 49° was used in Model A, B and C.

Figure 5. (a) Coseismic LOS range changes from CSK1; (b) Simulated interferogram from the best-fitting slip model; (c) Residual interferogram between (a) and (b). (d, e,

f) are similar to (a, b, c), but for azimuth displacements from the same pair.

Figure 6. Variation in S and P wave speed with depth for the Van region obtained from the Crust 2.0 database (http://igppweb.ucsd.edu/~gabi/crust2.html).

Figure 7. (a) horizontal GPS coseismic observations (white arrows) provided by Altiner *et al*. (2013) and simulated displacements using the Elastic half-space Earth model (red arrows), and Elastic layered Earth model (blue arrows).-(b) As for A, but for vertical displacements.

Figure 8. (a) Correlation between the projection of coseismic slip distribution on the surface (white lines) and topography. The arrows imply the projections of slips over the fault surface onto the surface. (b) the down dip force exerted by surface topography onto the fault plane where the effective coefficient of friction is set as 0.1. The broken lines show slip contours and grey arrows the associated vectors.

Figure 9. (a) Postseismic stress (grey arrows and dashed lines) overlaying the coseismic slip map. (b) Coseismic (solid lines) and postseismic (broken lines) slip contours overlaying the relative resistance exerted by topography.

Table 1 Details of InSAR pairs used in this study

Satellite	Index	Master-Slave(Date)	Baseline *	Signals**	Info
CSK	CSK1	20111010-20111023	192.8	COS	Range changes
CSK	CSK1			COS	Azimuth displacements
ASAR	ASAR	20101105-20111031	37.4	COS+POS	Range changes
CSK	CSK2	20111023-20111026	307.1	POS	Range changes
RS2	RS2	20111026-20111213	239.9	POS	Range changes

*: Perpendicular baseline represents the component of the orbital separation perpendicular to the radar line of sight, in meters.

**: COS denotes coseismic displacement signals, whilst POS represents postseismic displacement signals.

Table 2 Source parameters determined by different techniques

Def	Dataset	strike(°)	Lon	Lat	dip(°)	rake(°)	Length(km)	Width(km)	M_W[a]	Sources
GCMT	Seismic data	246	43.497[b]	38.691[b]	38	60	-	-	7.2	USGS[c]
Fielding	Seismic data	258	43.497[b]	38.691[b]	46	71	-	-	7.1	(Fielding et al., 2013)
Fielding	CSK & ASAR	259	43.497[b]	38.691[b]	42	-	-	-	7.13	As above
Irmak	Seismic data	246	43.3367	38.7188	46	59	-	-	7.13	(Irmak et al., 2012)
Elliott Model	CSK & ASAR	254	43.499	38.602	40	64	12	16.6	6.8	Elliott *et al.* (2013)
		254	43.329	38.593	55	93	12	8.9	6.8	
CSKU*	CSK Only	261.3	43.403[d]	38.702[d]	47.3	90	20.4	3.1	6.8	this study
CSKM*	CSK Only	261.3	43.403[d]	38.702[d]	49	88	40	40	7.03	this study
JointM	CSK & ASAR	261.3	43.403	38.702	49	90	40	40	6.99	this study

a, M_W was calculated using the formula given by Kanamori *et al.* (1975): $M_w = 0.75\log10(M_o) - 6.033$, where M_o is the seismic moment released during the earthquake. Different values of the shear modulus are used, 44 GPa in Fielding *et al.* (2013) and 32 GPa in this study.

b, the location of [lon,lat] represents the first motion determined by seismic wave data.

c, http://earthquake.usgs.gov/earthquakes/eqinthenews/2011/usb0006bqc/

d, the location here represents the central point of the top boundary of the fault which has been extended to the Earth surface.

*, Model CSKU was determined by the optimal CSK datasets using a uniform rectangular fault plane, whilst CSKM was the variable slip model based on the CSKU.

Figure

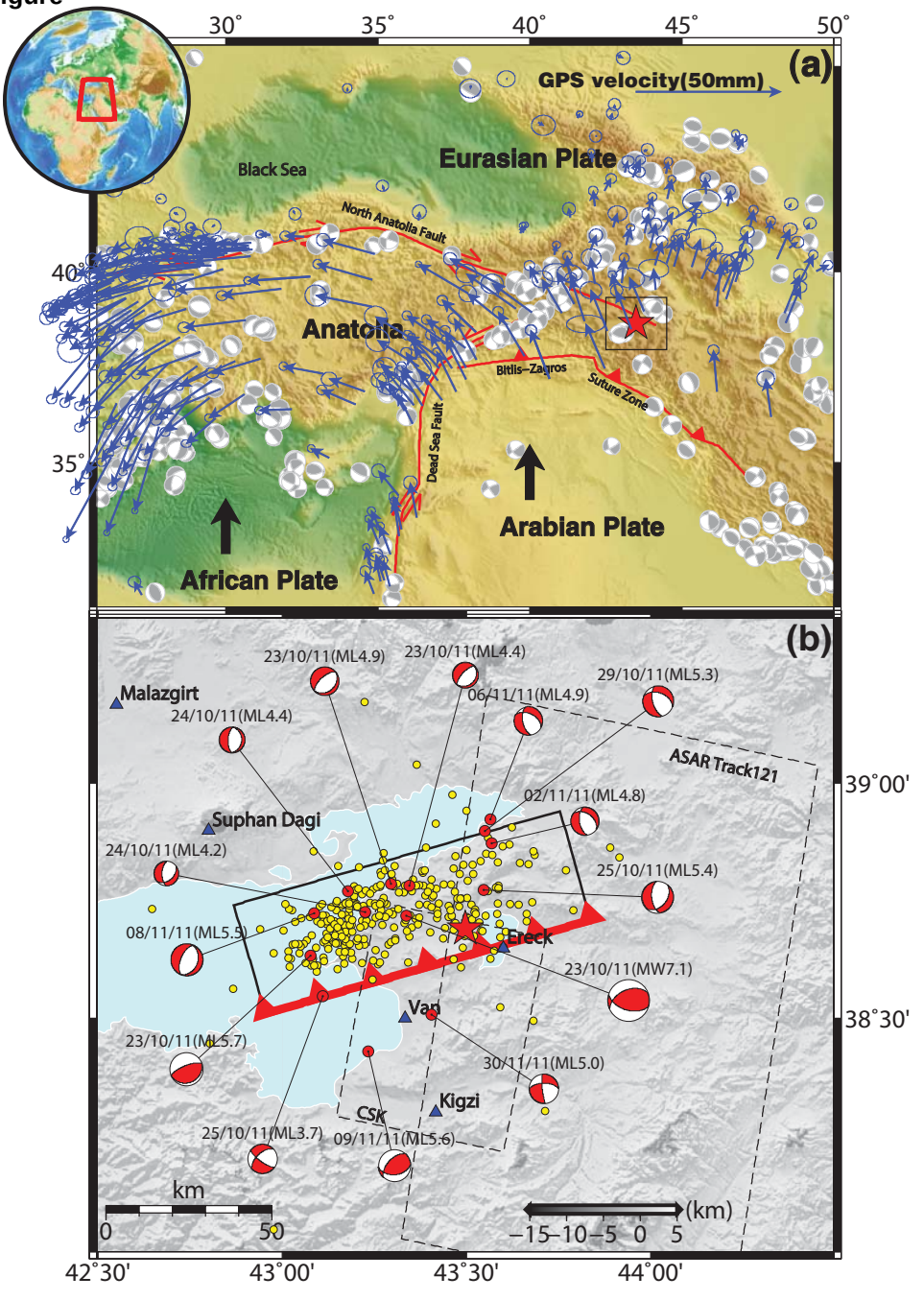

Feng et al. Fig 1

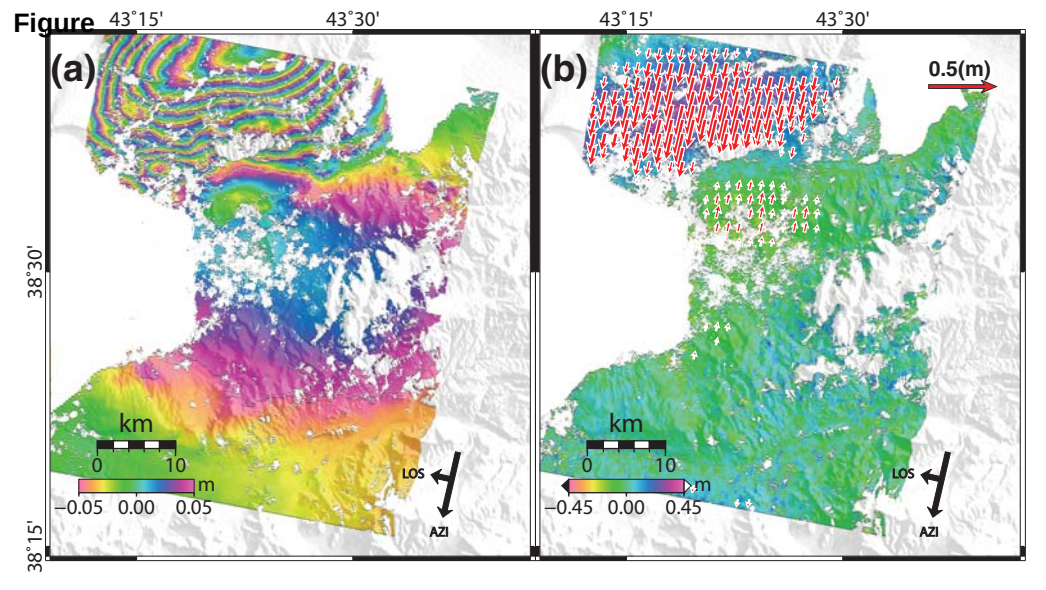

Figure 2 by Feng et al.

Figure

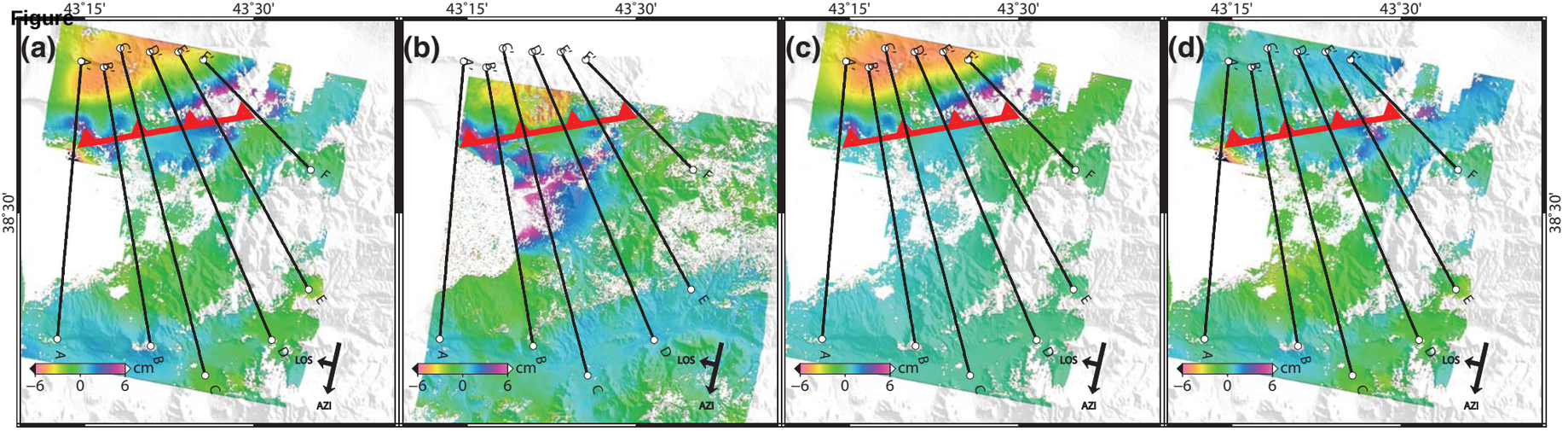

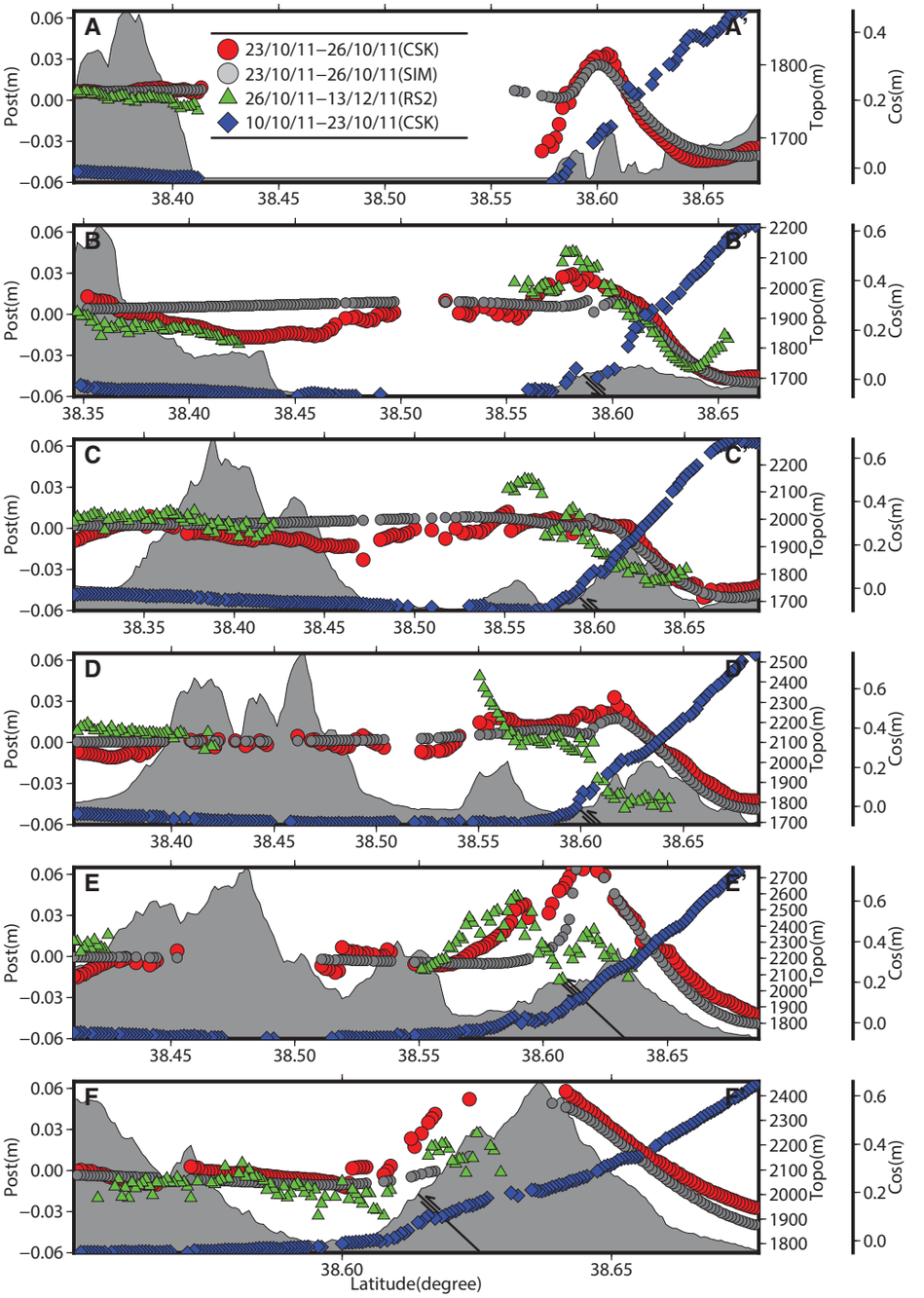

Figure 3 by Feng et al.

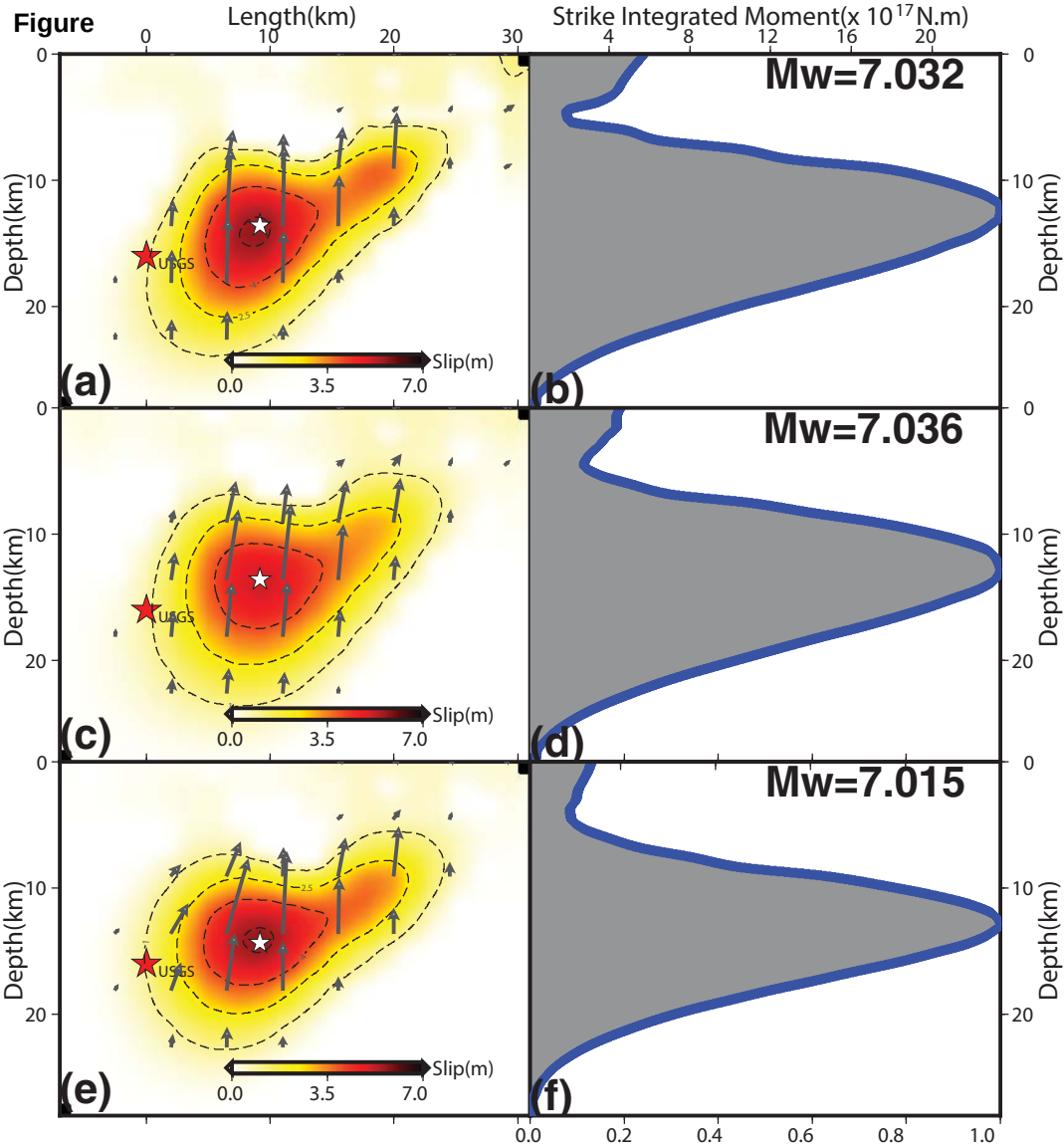

Figure 4 by Feng et al.

Figure

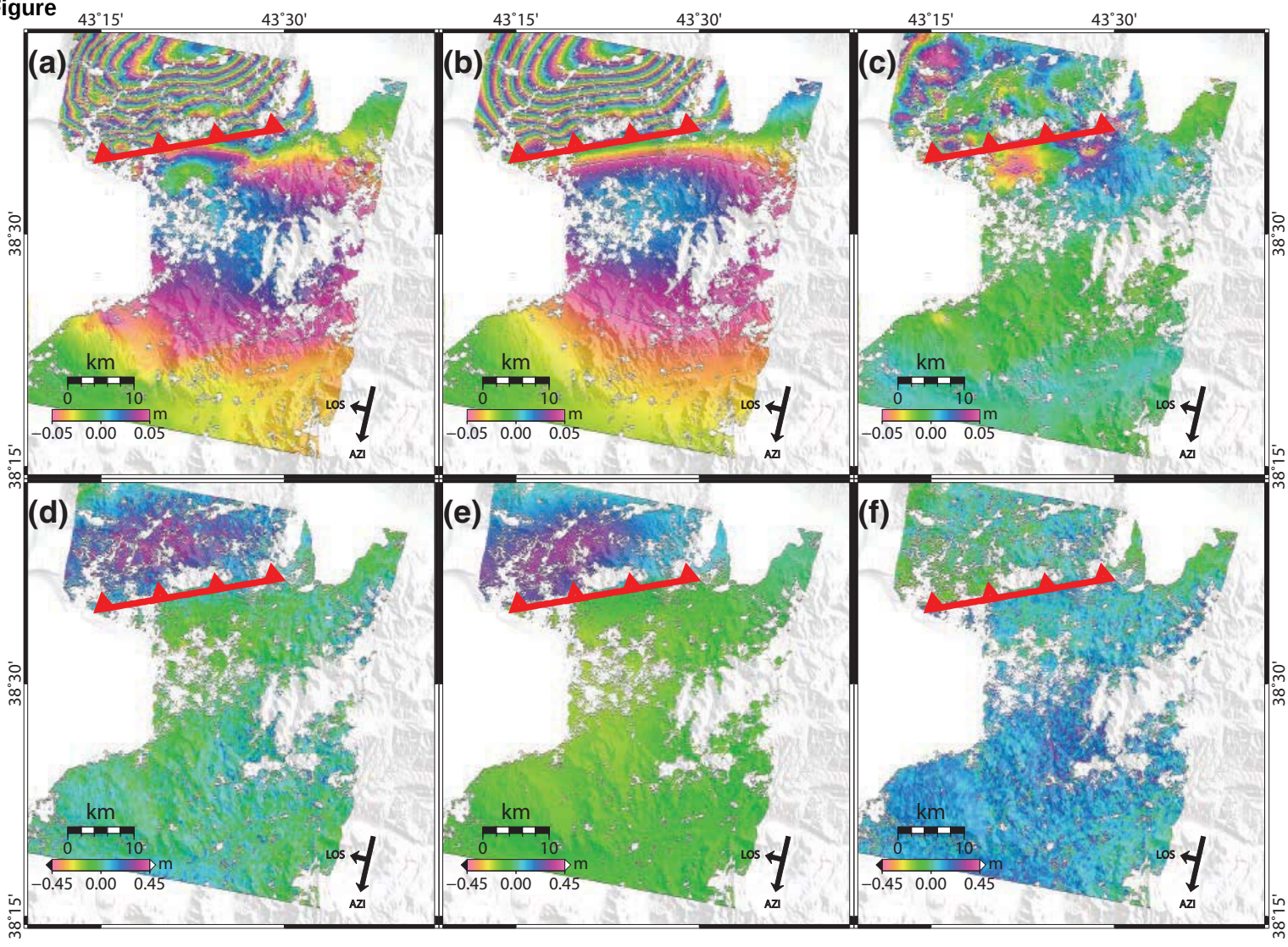

Figure 5 by Feng et al.

Figure

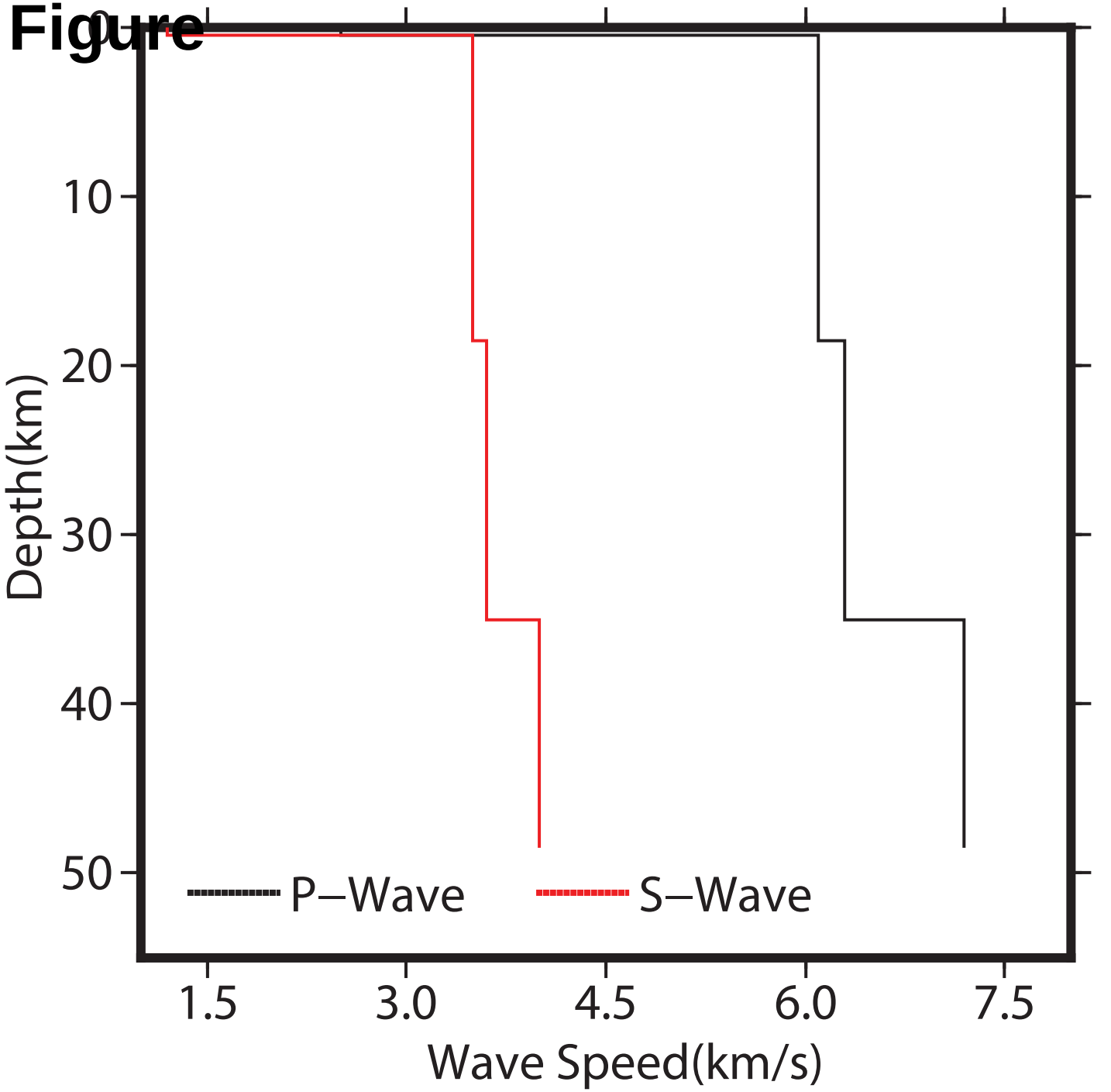

Feng et al, Fig6

Figure

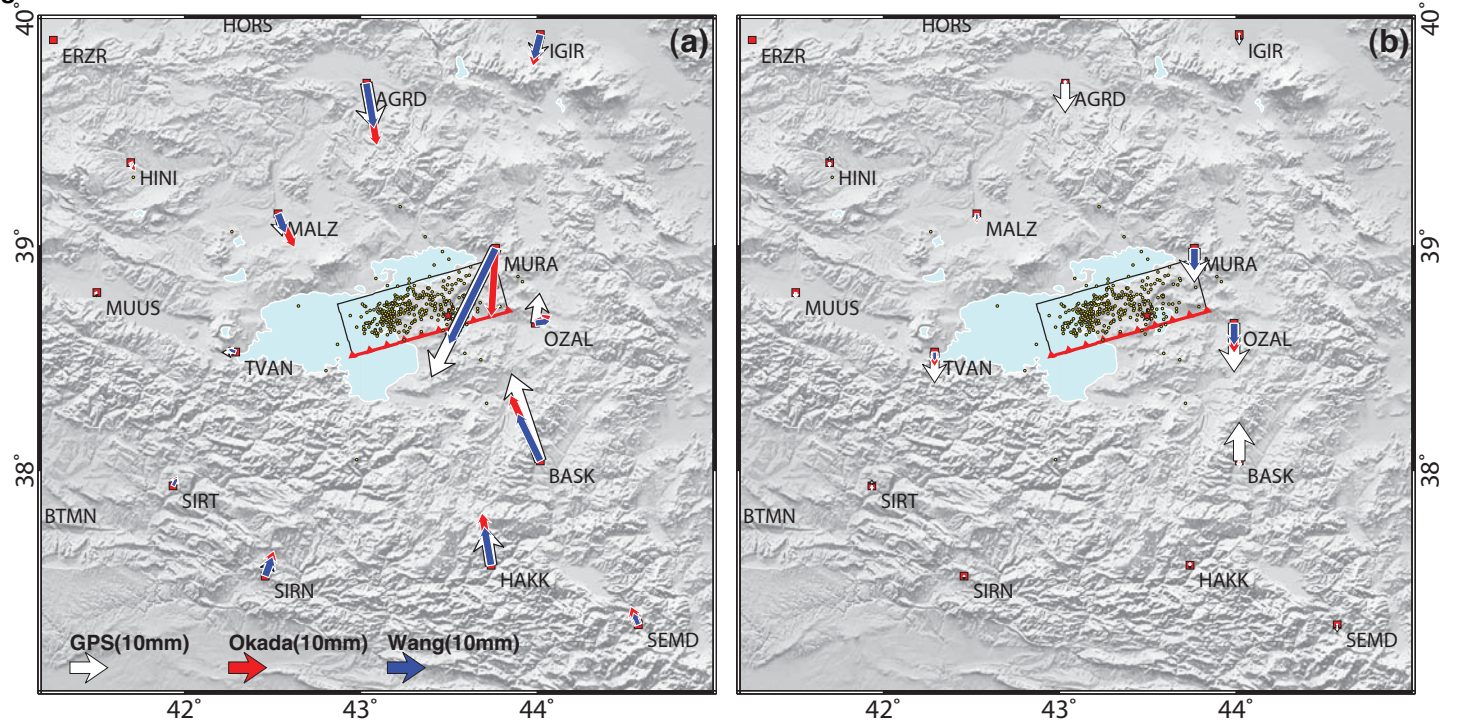

Figure 7 by Feng et al.

Figure

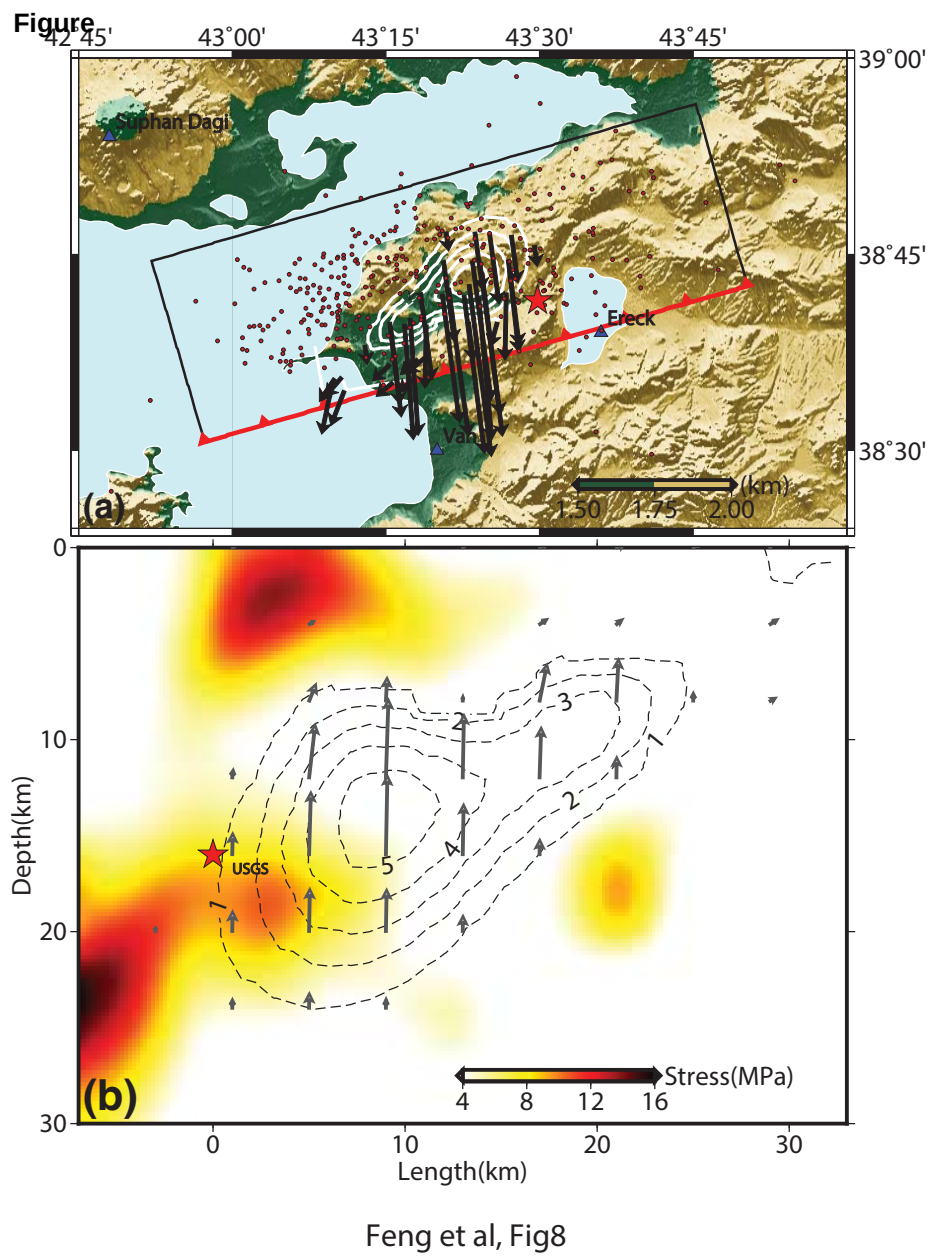

Feng et al, Fig8

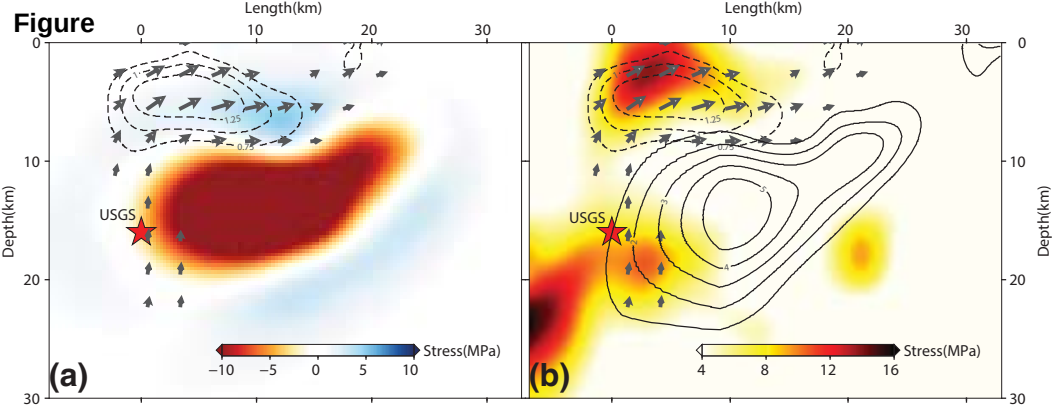

Figure 9 by Feng et al.

Supplementary material for online publication only

Click here to download Supplementary material for online publication only: Supplements_20140513_Fengetal.docx